ELSEVIER

Journal of Fluids and Structures 26 (2010) 218–235

JOURNAL OF FLUIDS AND STRUCTURES

www.elsevier.com/locate/jfs

Simultaneous measurements of velocity and deformation in flows through compliant diaphragms

D.M. Amatya[a,*], E.K. Longmire[b]

[a]*Department of Biomedical Engineering, University of Minnesota, 7-105 Hasselmo Hall, 312 Church St. SE, Minneapolis, MN 55455, USA*

[b]*Department of Aerospace Engineering & Mechanics, University of Minnesota, 110 Union St, SE, Minneapolis, MN 55455, USA*

Received 28 September 2007; accepted 28 September 2009
Available online 25 January 2010

Abstract

Flow through a circular orifice in a deformable diaphragm mounted in a pipe was studied experimentally as a simple yet suitable case for validating numerical fluid/structure interaction (FSI) codes including structures with significant deformation and strain. The flow was characterized using pressure taps, particle image velocimetry (PIV), and hot-film anemometry while deformation of the compliant diaphragm was determined directly from PIV images. The diaphragm material properties were measured independently by a uniaxial tensile testing machine. The diaphragm material modulus, orifice diameter, and pipe Reynolds number were varied over ranges appropriate for simulations of flows through heart valves. Pipe Reynolds numbers ranged from 600 (laminar upstream condition) to 8800 (turbulent upstream condition). The pressure drop across the diaphragm resulted in a concave deformation for all cases studied. For the range of Reynolds number tested, the Euler number decreased with increasing Reynolds number as a result of orifice expansion. The flow immediately downstream of compliant diaphragms was jet-like with strong inward radial velocity components and vena contracta. Laminar low Reynolds number flow ($Re = 600$) through both rigid and compliant diaphragms yielded early and regular roll up of coherent vortex rings at a fixed frequency in contrast to turbulent higher Reynolds number flow ($Re = 3900$), which yielded a broad range of vortex passage frequencies. Expansion of the compliant orifice for $Re = 3900$ resulted in an initially broader slower jet with delayed shear layer development compared with the equivalent rigid case.

Keywords: Fluid–structure interaction; Heart valve; Orifice flow; PIV; Deformable diaphragm; Jets

1. Introduction

Flows around and through flexible and deformable structures and vessels occur frequently in both industrial and physiological applications. Often, these flows are extremely complicated to model theoretically or numerically. For example, human heart valves are geometrically complex in shape, material, and dynamics. They include thin leaflets that can flex and strain significantly under loading of large pressure drops. The flow through the valves is typically unsteady and three-dimensional, including flow reversal, three-dimensional separation and vortex formation and

*Corresponding author. Tel.: +1 612 626 9504; fax: +1 612 626 1558.
E-mail address: amatya@umn.edu (D.M. Amatya).

0889-9746/$ - see front matter © 2009 Elsevier Ltd. All rights reserved.
doi:10.1016/j.jfluidstructs.2009.12.001

shedding (Yoganathan et al., 2005). All of these complexities are challenging to address individually, let alone collectively. Also, the inherent interaction between the flowing blood (generalized as a fluid continuum) and the valve (generalized as the deformable solid structure) requires coupling of the conservation of mass and momentum equations of fluids and solids. The solids equation must account for inhomogeneity, anisotropy, and non-linear material and geometric deformations of the three-dimensional valve. Meanwhile, the non-linear Navier–Stokes equations must handle three-dimensional variations in space and time. There is great interest in correctly modeling the fluid–structure interaction (FSI) in these flows as well as other flows that include structures or boundaries with significant deformation.

Numerous groups (Carmody et al., 2006; Cheng et al., 2003; de Hart et al., 2000, 2003) have considered and developed FSI models for heart valve applications. The arbitrary-Lagrangian–Eulerian (Carmody et al., 2006; Cheng et al., 2003), immersed boundary formulation (Lemmon and Yoganathan, 2000), and fictitious domain methods (de Hart et al., 2000, 2003) are current approaches to handling the FSI problem. Carmody et al. (2006) used the arbitrary Langrangian–Eulerian (ALE) algorithm for a three-dimensional FSI model of an ideal aortic valve as defined by Thubrikar (1990). They compared the spatial and temporal opening/closing of porcine valve leaflets in a pulse duplicator system to their computational results of an idealized aortic valve with three deformable leaflets. They showed good qualitative correspondence, but suggested that detailed quantitative comparison was inappropriate. Cheng et al. (2003) tracked temporal leaflet position of a rigid mechanical valve simulating a single closing event using a two-dimensional ALE algorithm. They compared the numerical and experimental results and showed that the trend in opening angle versus time was similar, but that the numerical opening angle lagged in time. They attributed the discrepancy to three-dimensionality in the experiment.

de Hart et al. (2000), using their fictitious domain method, performed two-dimensional simulations of a flexible leaflet in a rigid sinus cavity under pulsatile flow. For experimental validation, they observed a rectangular rubber (EPDM) sheet mounted within a pulse duplicator system. The sheet exhibited some deflection perpendicular to the viewing plane due to three-dimensional motion in the flow. A thicker, stiffer leaflet yielded motion that was more two-dimensional. The leaflet motion and fluid flow, measured by laser Doppler velocimetry, were well predicted by the simulation. The fluid velocity patterns were similar for both numerical and experimental cases with the exception of a secondary vortex near the leaflet fixation point present only in the numerical case that was attributed to a mesh refinement issue.

Stijnen et al. (2004) followed up this study by examining a two-dimensional rotating Lexan leaflet (de Hart et al., 2000). Particle image velocimetry (PIV) was used to determine velocity fields. Once again, the trends in leaflet motion were similar in the experiments and computations. Discrepancies in leaflet motion were attributed to the boundary layer flow near the sidewalls of the experimental set-up, which did not exist in the two-dimensional simulation. The computed and experimental flow patterns were very similar, although some discrepancies resulted from the difference in the valve motion. The same experimental approach was used to validate additional numerical simulations of flow through rigid valves (Dumont et al., 2004; Kaminsky et al., 2007). Separately, Ge and Sotiropoulos performed three-dimensional direct numerical simulation on flow through mechanical bileaflet valves using experimental data to prescribe the leaflet kinematics (Dasi et al., 2007).

These groups have made significant progress in development of FSI codes for simulation of physiological conditions. However, most of the previous results considered structures or geometries in which elastic strain was either limited or not easily quantified. The current investigation was motivated originally by the need for test data to validate a multigrid method (Lui et al., 2007) that includes thin structures (e.g. valve leaflets) subject to significant flow-induced strain. Therefore, we consider a problem with relatively simple initial and boundary conditions that allows for flow three-dimensionality and unsteadiness: Fully developed pipe flow with significant Reynolds number approaches and passes through a circular orifice in a deformable diaphragm. The diaphragm material is homogeneous and isotropic. The diaphragm-in-pipe-flow has the premise that the upstream flow affects the state of the deformable diaphragm, and the diaphragm state affects the downstream flow. In our experiments, we seek to quantify both the diaphragm deformation and fluid motion for a number of parameter sets.

Compression-molded silicone serves as the flexible diaphragm, and the deformation is quantifiable *in situ*. Varying the silicone material properties, which are measured independently, allows adjustment of the diaphragm compliance. Additionally, the pipe flow Reynolds number and diaphragm orifice area are varied. Reynolds numbers yielding significant deformation and strain are considered. In the following sections, we describe our experiments designed to quantify the effects of these parameters on the resulting orifice deformation and flow characteristics. In addition, we provide detailed data as well as initial and boundary conditions suitable for validation of FSI codes.

2. Methods

2.1. Flow facility

An acrylic pipe with an inner diameter D of 2.54 cm, a wall thickness of 0.3 cm, and a length of 170.2 cm was used (Fig. 1). These dimensions were chosen to match approximate aorta diameter, minimize optical distortion, and ensure

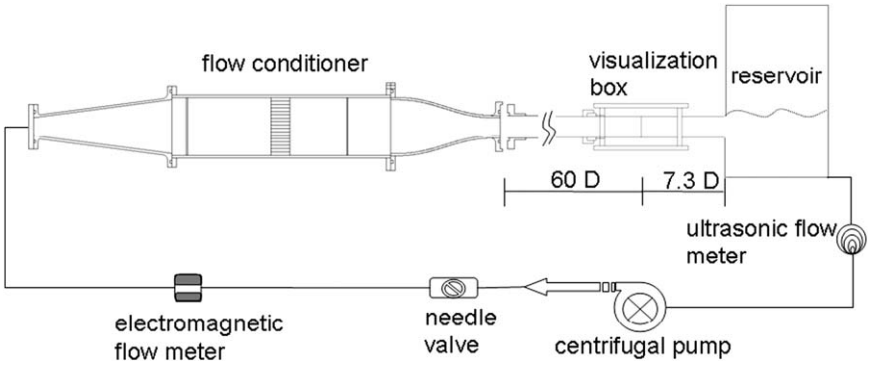

Fig. 1. Experimental flow configuration. Figure is not drawn to scale.

the flow through the pipe was fully developed, respectively. The pipe was sectioned to mount the diaphragm 152.4 cm (60D) downstream of the entrance and 18.6 cm (7.3D) upstream of a flow reservoir. A visualization box was placed external to the pipe at the location of the diaphragm. The box was filled with sodium iodide solution of which the refractive index was matched to that of the acrylic pipe (~1.5) resulting in minimal optical distortion caused by the wall curvature.

A flow conditioner (Fig. 1) was located upstream of the pipe section to minimize disturbances. The flow conditioner included three components. First, the unconditioned flow entered a diffuser with inlet diameter of 2.54 cm, outlet diameter of 7.62 cm, and length of 19.5 cm. Next, the flow passed through a 30.5 cm length settling chamber containing a perforated plate with holes of 12 mm diameter, a honeycomb section with 0.2 cm diameter tubes and 2.5 cm length, and a stainless steel screen (mesh size 2 mm). These components acted to eliminate swirling motion and decrease flow non-uniformity over the cross-section. Finally, the conditioned flow passed through a nozzle with diameter ratio of 3:1. The contraction followed a 5th-order polynomial fit which ensured smooth transition of the working fluid into the pipe section.

A centrifugal pump drove the working fluid (0.9% by weight NaCl solution, $\rho = 1.005\,\mathrm{g/cm^3}$, and $\eta \sim 1.02$ mPa s), and the flow rate was controlled by a needle valve. A Carolina Medical electromagnetic flow meter with $\pm 5\%$ accuracy when operating at 3–5 L/min, positioned inline upstream of the flow conditioner, was used to monitor the steady volumetric flow rates. Additionally, a Transonic Systems ultrasonic flow meter (4% absolute accuracy of the 2 L/min full-scale) external to the flow was used to monitor flow rates at low Reynolds numbers. Pressure taps were located one diameter upstream and downstream of the diaphragm location. Vivitro Systems Inc. transducers monitored pressures with an accuracy of 1 mmHg. An additional differential pressure transducer having an accuracy of 0.1% of the 0.75 mmHg full-scale (Druck Incorporated) was used at low flow rates.

2.2. Diaphragms

Fig. 2(a) and (b) show a sample diaphragm and a schematic representation of its mounting within the pipe, respectively. Two-part silicone gels (Nusil Technology) were chosen for the diaphragm material based on the high manufacturer-stated compliance of the cured product. Three gel combinations: MED 4901 (most compliant), MED 4905, and MED 4-4220 (least compliant) were tested. The silicone gels were compression-molded in an aluminum cavity and cured at 400 °F for 20 min resulting in circular diaphragms as shown in Fig. 2(a). Each diaphragm had 2.54 cm diameter and 0.1 cm thickness with an outer ring of 0.3 cm thickness for mounting between adjacent acrylic pipe sections as shown in Fig. 2(b). An orifice of diameter d was punched out from the center of each diaphragm. Most tests were performed with $d/D = 0.31$, which yielded measurable deformations for the lowest volumetric flow rates examined. For a comparison case, a rigid aluminum diaphragm with 0.3 cm thickness and $d/D = 0.31$ was used. One compliant diaphragm with a larger orifice ($d/D = 0.69$, MED 4901) was also tested. In total five diaphragms were tested (MED 4901 with $d/D = 0.31$, MED 4905 with $d/D = 0.31$, MED 4-4220 with $d/D = 0.31$, aluminum with $d/D = 0.31$, and MED 4901 with $d/D = 0.69$). Pressure drop, flow rate, and diaphragm deformation data were acquired for five diaphragms: MED 4901, MED 4905, and MED 4-4220, and rigid with $d/D = 0.31$, and MED 4901 with $d/D = 0.69$. Detailed PIV and hot-film anemometry measurements were performed on the MED-4901 and rigid diaphragms.

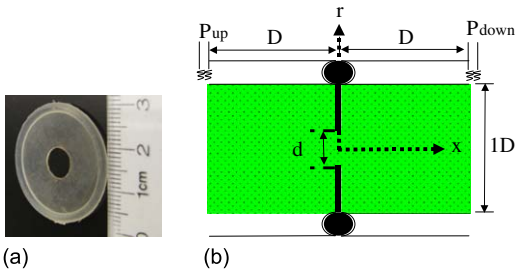

Fig. 2. (a) Picture of the silicone diaphragm. (b) Diaphragm set up, pressure tap locations, and coordinate system. The outer-ring of the diaphragm is used to situate it between the two neighboring acrylic sections.

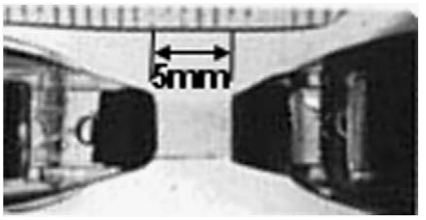

Fig. 3. Experimental silicone sample held by compression grips.

2.3. Tensile testing of compliant materials

Rectangular samples of each silicone type were cut from molded diaphragms and tested. Uniaxial tensile tests were performed with a material testing system (Instron Corp., Canton, MA). Each sample was placed in compressive grips as shown in Fig. 3. The nominal gauge length (distance between grips) was measured and used to determine engineering strain (ε). The samples were subjected to a 0.05 N preload and strained at 1%/s increments until reaching a total strain ε of 50%. A 5 ± 0.00125 N load cell recorded the corresponding force applied. The force value was normalized by the initial sample cross-sectional area (thickness × width) to obtain a corresponding engineering stress (σ). A neo-Hookean hyperelastic model for incompressible material,

$$\sigma = \mu(\varepsilon - (\varepsilon + 1)^{-2} + 1) \tag{1}$$

was fit to the averaged ($N = 4$) stress–strain data for each silicone material type. A shear modulus (μ) was then extracted by minimizing the sum-of-squares for each material type.

2.4. Flow measurements

Pressure, deformation, and flow-rate measurements were carried out over a range of pipe Reynolds numbers Re = 600–8800 based on the average velocity over the pipe cross-section U_{bulk} and the pipe diameter D. Detailed velocity field measurements were obtained for two volumetric flow rates of 0.7 L/min (Re = 600) and 4.7 L/min (Re = 3900) corresponding with fully developed laminar (Poiseuille) and turbulent flow upstream of the small orifice ($d/D = 0.31$) diaphragm, respectively. Both Reynolds numbers yield significant diaphragm deformation and are within the physiological range (Stein and Sabbah, 1976). Additional velocity fields were acquired for flow through the larger orifice diaphragm ($d/D = 0.69$) at 10.5 L/min (Re = 8800) with the similar intent of producing significant diaphragm deformation.

Particle image velocimetry was conducted approximately $8D$ upstream of the diaphragm location to quantify initial conditions and immediately downstream of each diaphragm to obtain instantaneous and ensemble-averaged velocity fields. For the PIV measurements, 10 μm hollow spherical glass beads (1.05–1.15 g/cm^3) were seeded into the working fluid. The flow and beads were illuminated by pulsed light sheets from a pair of Nd:YAG lasers ($\lambda = 532$ nm) aimed downward through the pipe cross-section. Each laser beam passed through a combination of 25 mm focal length cylindrical and 200 mm focal length spherical lenses resulting in sheets of approximately 1 mm thickness. Images were acquired by a dual-frame camera (TSI Powerview 4 M) with a resolution of 2048 × 2048 pixels and 12-bit dynamic

range. A 200 mm lens (Nikon micro-Nikkor) was mounted on the camera and located approximately 30 cm from the light sheet resulting in a magnification factor $M = 55$ pixels/mm. An aperture setting of $f\#$ 5.6 allowed sufficient illumination for particle identification at a laser intensity of 80 mJ/pulse. Pairs of images separated by the laser pulse separation time (τ) and focused on the laser sheet plane were recorded.

Ensembles of image pairs were acquired for each run so that averaged quantities could be determined. The number of image pairs was 500 for all measurements upstream of the diaphragm, 275 for Re = 600, 550 for Re = 3900, and 825 for Re = 8800 downstream of the diaphragm. Image pairs were acquired at a repetition rate of 1–2 Hz so that consecutive image pairs could be considered statistically independent. TSI INSIGHT3G software was used to process the data. Initially, the raw images were conditioned by a minimum average pixel intensity filter, which diminishes the effects of background light, laser glare, and noise. Velocity vectors were determined from 64×64 pixel interrogation areas with 50% overlap. This corresponded to a vector spacing of 0.06 cm in a field of view of approximately 2.54 cm × 2.54 cm resulting in approximately 40×40 vectors per field. A maximum vector displacement of approximately 8 pixels was set by adjusting τ for each case in accordance with the 25% in-plane particle displacement rule (Keane and Adrian, 1990). A multipass central difference image correction deformation algorithm with 0.1 pixel displacement accuracy (Wereley and Gui, 2001) was used for PIV processing. Spurious vectors in each pass were identified and eliminated using a 2-pixel displacement 5×5 local median filter with missing vectors were interpolated using a 3×3 mean interpolation. The processing resulted in 97% or higher valid vectors. Based on the pixel displacement accuracy, the uncertainty in a given velocity vector in the upstream data was 3.5% and 8% of U_{bulk} for Re = 600 and Re = 3900, respectively. The uncertainty in a given vector in all downstream data was about 20% of U_{bulk}.

Since the PIV system provided only instantaneous views of flow downstream of each diaphragm, hot-film anemometry was performed to provide additional point-measurements of power spectra. A Dantec hot-film probe was inserted through a hole in the pipe section at $x/D = 0.9$ and positioned in the developing shear layer downstream of a given diaphragm. The radial location was chosen as that which yielded the strongest fluctuation energy. The probe was operated in constant temperature mode at an overheat ratio of 1.2 and attached to an anemometer from AA Lab Systems (AN-1003). The sampling rate of 1000 Hz (f_s) resulted in a Nyquist frequency of 500 Hz, sufficient for resolving the fluctuation energy at the Reynolds numbers tested. A total of $N = 130\,172$ data points were acquired for each case, and power spectra were computed using Matlab.

2.5. Diaphragm deformation measurements

Deformation of the diaphragm was recorded by the PIV camera. The two-dimensional outline of the deformed diaphragm was extracted with ImageJ 1.34 s (National Institutes of Health) using the "Find Edges" kernel, which highlights sharp changes in intensity. The uncertainty in identifying the downstream edge of the diaphragm is about 5 pixels (0.09 mm = 0.0035D). The deformed shapes for all three silicone diaphragm materials were recorded along with the corresponding flow rates and pressure drops.

3. Results

In the following sections, the streamwise and radial directions of the flow are represented by the cylindrical (x, r) coordinate system shown in Fig. 2(b) with the origin located on the pipe centerline and coincident with the streamwise location of the undeformed diaphragm. The streamwise and radial velocity components are denoted as U and V respectively, with $V > 0$ corresponding with outward radial velocity.

3.1. Diaphragm tensile testing

The engineering stress versus strain curves, obtained from the uniaxial tensile testing (see Fig. 3), are shown in Fig. 4 for the three silicone materials. For each condition, the mean of four measurements is plotted. Individual measurements deviated from the mean values by less than 12%. A neo-Hookean material model was curve-fit, and shear modulus values (μ) of 0.016, 0.03, and 0.11 MPa were obtained for MED 4901, MED 4905, and MED 4-4220, respectively. These values correspond to a Young's modulus of 0.048, 0.09, and 0.33 MPa, which are of similar order to values measured in native aortic valve leaflets (Clark, 1973; Mavrilas and Missirlis, 1991). According to the results in Fig. 4, within the range of strain $0 < \varepsilon < 0.5$, a neo-Hookean model is sufficient for the three MED materials.

3.2. Diaphragm deformation in pipe flow

Fig. 5 shows a side view representation of the deformation for the MED 4901 compliant diaphragm ($\mu = 0.016$ MPa, $d/D = 0.31$) at Re = 600, 3900, and 8800. For all Reynolds numbers examined, the diaphragm location was steady and did not vary in time due to fluctuations in the flow. Note that the diaphragm could not be observed from $x/D = 0$–0.04 due to the visual obstruction created by the mounting ring. The diaphragm has a concave deformation with respect to the upstream flow. The undeformed orifice radius is $0.16D$. At the lowest Reynolds number of 600, the axial deflection of the diaphragm tip ($\Delta x/D = 0.07 \pm 0.0035$) is more prominent than the radial orifice expansion ($\Delta d/D = 0.015 \pm 0.0035$). As Re increases to 8800, however, the radial expansion ($\Delta d/D = 0.20 \pm 0.0035$) becomes comparable to the axial deflection ($\Delta x/D = 0.24 \pm 0.0035$). For this diaphragm, the circumferential strain at the location of the orifice ($\Delta d/d$) increases with Reynolds number as shown in Fig. 6. In general, the higher modulus diaphragms, not shown, deformed less at like Reynolds numbers, but exhibited similar concave shapes. The concave shape occurred also when the orifice size was increased (e.g. $d/D = 0.69$).

Plots of normalized pressure drop (Euler number) versus flow rate (Reynolds number) are shown in Fig. 7 for the four diaphragms with $d/D = 0.31$. The Euler number is defined as

$$\mathrm{Eu} = \frac{p_{\mathrm{up}} - p_{\mathrm{down}}}{0.5\rho U_{\mathrm{bulk}}^2}. \tag{2}$$

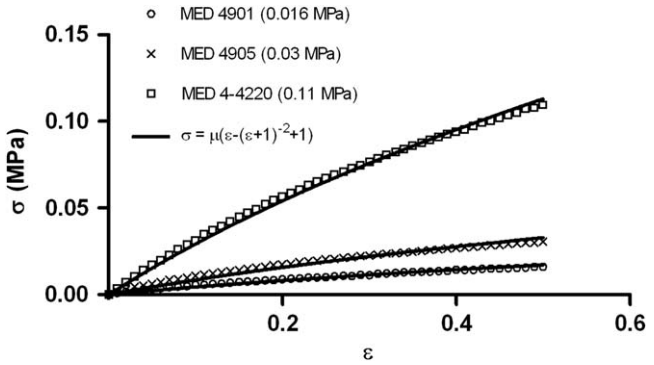

Fig. 4. Uniaxial tensile tests of rectangular silicone diaphragm samples. A neo-Hookean material model is curve-fit for MED 4901 ($\mu = 0.016$ MPa), MED 4905 ($\mu = 0.03$ MPa), and MED 4-4220 ($\mu = 0.11$ MPa).

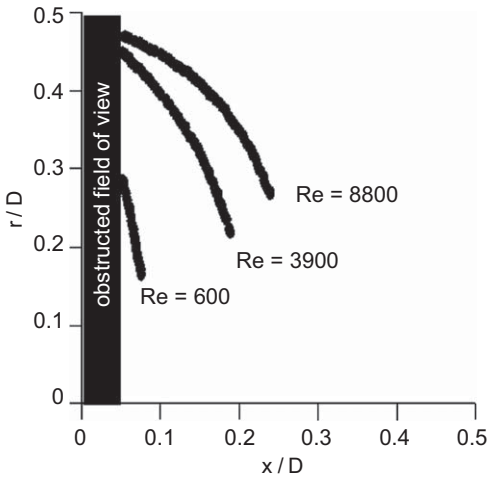

Fig. 5. Diaphragm ($\mu = 0.016$ MPa) deformation state for three Reynolds numbers, $d/D = 0.31$.

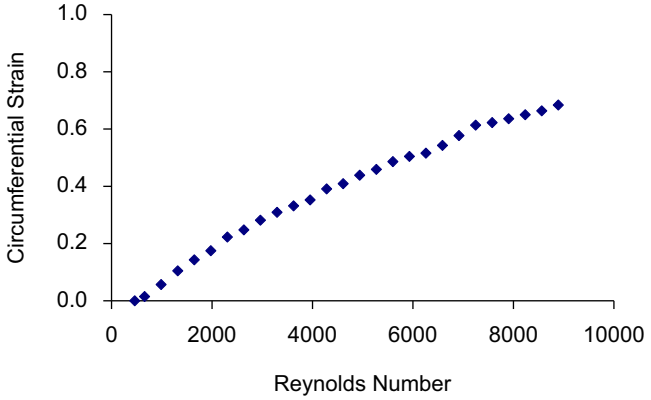

Fig. 6. Circumferential strain ($\Delta d/d$) measured at the diaphragm ($\mu = 0.016$ MPa) orifice versus Reynolds number, $d/D = 0.31$.

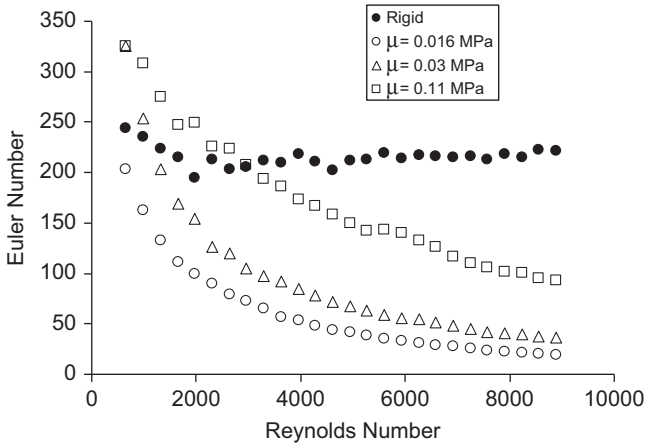

Fig. 7. Normalized pressure drop versus Reynolds number, $d/D = 0.31$.

For the rigid diaphragm, the Euler number is independent of Reynolds number over this range, and the value of Eu∼200 is consistent with findings by Morrison (2003) for $d/D = 0.31$. For the compliant diaphragms (open symbols), however, the Euler number decreases with increasing Reynolds number. Additionally, as the diaphragm compliance increases (μ decreases), the Euler number decreases more strongly. From Figs. 5 and 6, it is clear that Euler number decreases because of orifice expansion.

To account for this expansion, we can calculate a discharge coefficient (C_d) as the ratio of actual flow rate through the orifice to the ideal (or potential) flow rate based on the measured pressure drop. In this case, we assume that our measured pressure drop equals the difference between the pressure upstream of the orifice and the pressure at the orifice location. The measured pressure difference includes losses mainly due to flow separation upstream, friction, and turbulence. Fig. 8 shows C_d versus Reynolds number for the rigid and the most compliant ($\mu = 0.016$ MPa) diaphragms with $d/D = 0.31$. In the range $170 < \mathrm{Re} < 680$, the Druck differential pressure transducer and Transonic ultrasonic flow meter were used, and in the range $990 < \mathrm{Re} < 8800$, the Vivitro pressure transducers and Carolina Medical electromagnetic flow meter were used. The results, plotted with error bars, suggest that the stated uncertainty in the Vivitro/Carolina Medical measurements is larger than the actual uncertainty, so that the results in the range $990 < \mathrm{Re} < 3000$ appear reasonably accurate. Since C_d is calculated based on the actual orifice area at each Reynolds number, its value remains fairly constant, in fact it decreases slightly over the range studied for both the rigid and compliant diaphragms. The C_d values for the rigid diaphragm are similar to those reported in the literature in which P_{down} was located at $x/D = 0.5$ (Perry et al., 1984). Interestingly, the compliant diaphragm ($\mu = 0.016$ MPa) has a smaller discharge coefficient at all Reynolds numbers, indicating a smaller efficiency or a larger pressure loss. Although the curved diaphragm shape might be expected to decrease upstream separation near the pipe wall (and therefore

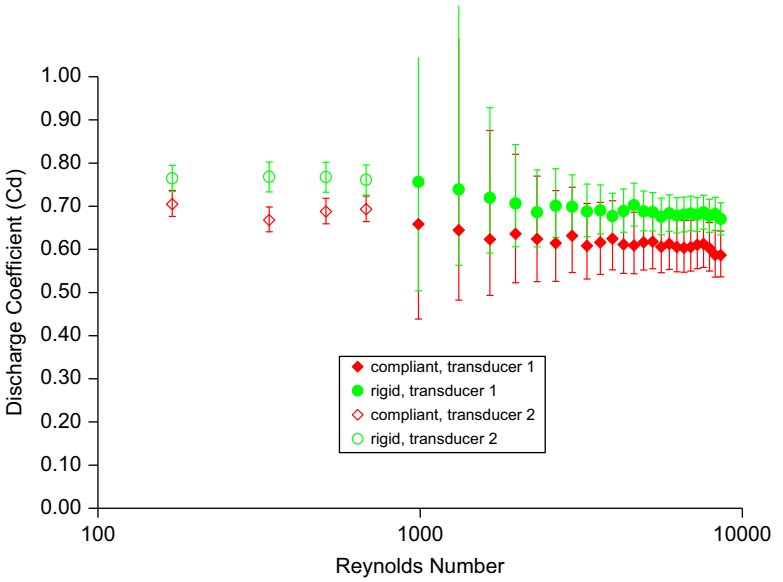

Fig. 8. Discharge coefficient of the compliant ($\mu = 0.016$ MPa) and rigid diaphragms for Reynolds number range of 170–8800, $d/D = 0.31$. Low range (Re = 140–680) and high range (Re = 990–8800) were acquired using separate pressure and flow rate instrumentation.

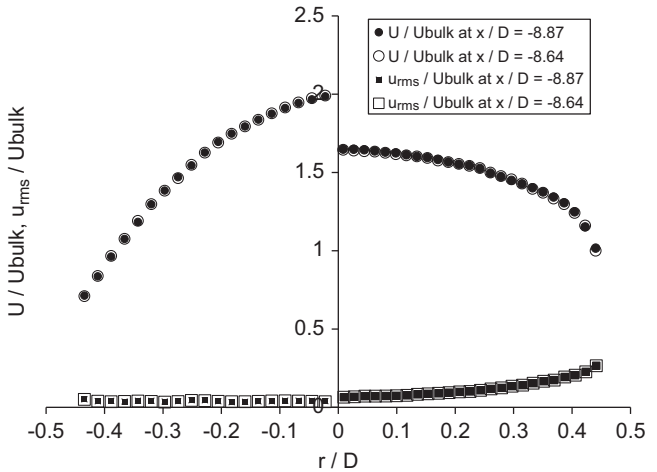

Fig. 9. Upstream mean streamwise and u_{rms} velocity profiles for Re = 600 (left) and Re = 3900 (right).

increase C_d), the fact that C_d decreases suggests that the curved shape may generate a stronger vena contracta than the flat rigid orifice (see velocity results below).

3.3. Initial conditions and upstream velocity profiles

PIV velocity fields acquired upstream of the diaphragm were averaged over the 500 samples for both Re = 600 and 3900. All velocities are normalized by U_{bulk}. The mean and rms streamwise velocity profiles are shown in Fig. 9 at two streamwise locations for both Re = 600 (left) and Re = 3900 (right). For Re = 600, the mean curve, U/U_{bulk}, resembles Poiseuille flow (circles). The two streamwise locations plotted ($-8.87D$ and $-8.64D$) indicated by the open and solid circles show excellent overlap. The rms velocity, values u_{rms}/U_{bulk}, plotted as squares, are also small as expected for the laminar flow, and result mainly from uncertainty in the PIV correlations. For Re = 3900, the mean streamwise profile is

blunter as is characteristic for turbulent flow. Again, the profiles overlap for the two streamwise locations, indicating that the shape is not changing with increasing streamwise distance. Near the centerline, the measured rms values are dominated by variations due to uncertainty in the PIV measurements, However, the peak u_{rms}/U_{bulk} level is shown in Fig. 9 to be 0.23 at $r/D = 0.44$. This value is significantly larger than at Re = 600, which should be expected for turbulent flow. Note that error bars were not plotted because they span a range smaller than the size of the corresponding symbols.

3.4. Downstream flow fields

Fig. 10 shows mean velocity vectors at five streamwise locations for four flow cases. Each plot also includes gray-scale contours of the streamwise rms velocity (u_{rms}) throughout the measurement field. In the literature considering flow through nozzles or orifices, displacements and velocities are typically scaled by the orifice diameter d and the mean jet velocity through the orifice U_{jet}. In the current study, however, all data are normalized by the pipe diameter D and the mean pipe velocity U_{bulk} since the orifice-based scales vary with Re and diaphragm compliance. The four cases: Re = 600 and rigid diaphragm, Re = 600 and compliant diaphragm, Re = 3900 and rigid diaphragm, and Re = 3900 and compliant diaphragm are labeled as LR, LC, TR, and TC in subsequent discussion. Note that the deformed diaphragm positions are also plotted in the LC and TC cases. The statistical uncertainties in U and u_{rms} near the jet centerline for all four cases were $0.03U_{bulk}$ and $0.02U_{bulk}$, respectively.

In Fig. 10(a), the LR case yields jet-like flow downstream of the orifice with a relatively uniform profile for $r/D < 0.16$ at $x/D = 0.15$. At larger radii, the velocity magnitude decreases suggesting the presence of a shear layer already near $x/D = 0$. The jet profile widens as the shear layer spreads becoming more Gaussian in shape. The values of u_{rms}/U_{bulk} are large across a relatively narrow layer up to $x/D = 0.45$. Beyond this location, the layer of significant rms values spreads rapidly. The relatively sudden spread suggests the rapid growth of instabilities and presence of vortical structures in the shear layer. This growth occurs relatively early compared with growth in jets exiting contoured nozzles (Crow and Champagne, 1971). By $x/D = 0.65$, u_{rms} is significant all the way to the centerline.

The LC results in Fig. 10(b) are somewhat similar to those observed for LR in that a jet-like flow ensues downstream of the orifice. A key difference, however, is a significant inward radial velocity (indicated by inward pointing vectors)

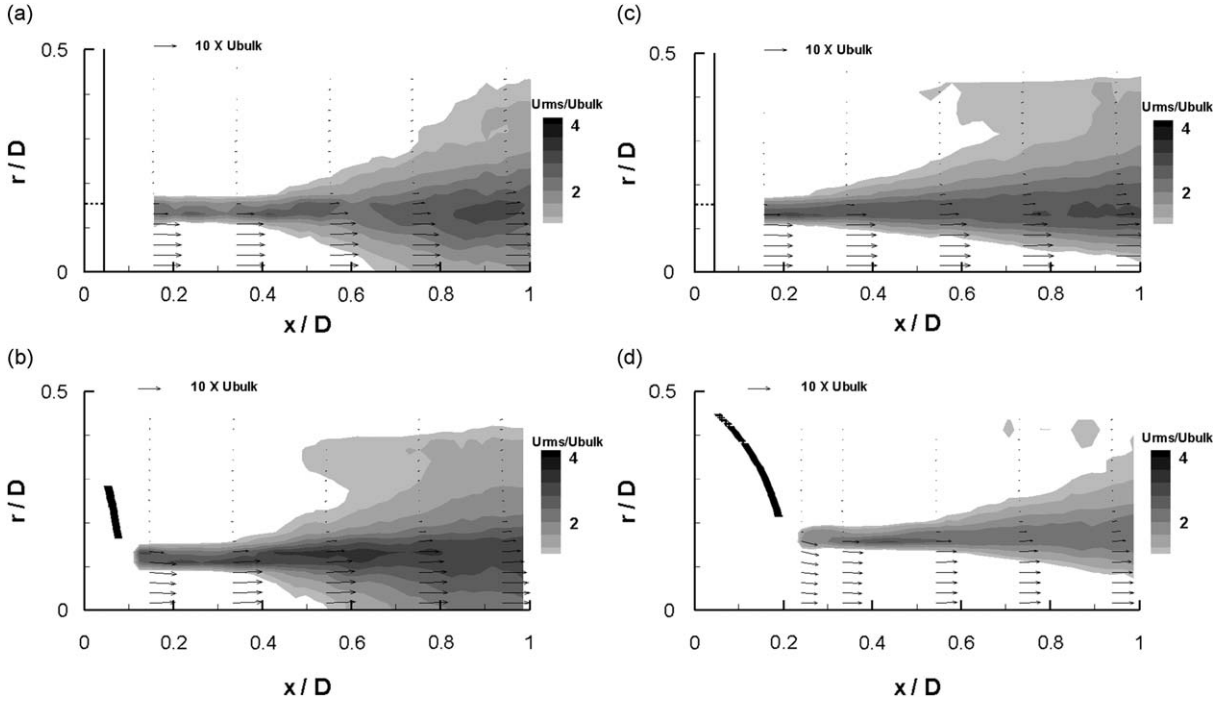

Fig. 10. Downstream mean velocity vectors with u_{rms}/U_{bulk} contours. Lowest contour plotted is $u_{rms}/U_{bulk} = 1$. Contour increments are 0.13: (a) LR: Re = 600, $d/D = 0.31$; (b) LC: Re = 600, $d/D = 0.31$; (c) TR: Re = 3900, $d/D = 0.31$; and (d) TC: Re = 3900, $d/D = 0.31$ and $d_{eff}/D = 0.42$. Diaphragm locations are superposed.

immediately downstream of the orifice, indicating a vena contracta effect caused by the concave diaphragm shape. (this radial velocity is quantified in Fig. 11(b) described below). Also, the streamwise velocity is lower at the centerline than at $r/D = 0.15$. By $x/D = 0.34$, the mean velocity profile has become more uniform for $r/D \leq 0.15$, and the inward component has disappeared. In fact, the vectors have a small outward component. The rms contours in Fig. 10(b) indicate that disturbances grow faster in the LC case than in the LR case. Note that $u_{rms}/U_{bulk} > 1$ already at $x/D = 0.55$ for LC, and further downstream, u_{rms}/U_{bulk} is larger both along the centerline and close to the pipe wall for LC than for LR.

For turbulent upstream conditions, the mean velocity profile near the rigid orifice exit (TR in Fig. 10(c)) is similar to the LR case. However, the shear layer spreads outward earlier, already by $x/D = 0.25$, as indicated by the broadening of the u_{rms} contours. Unlike in both of the low Reynolds number cases, the u_{rms}/U_{bulk} values remain small near the centerline to the limit of the field of view. The rms results overall indicate possible earlier growth of instabilities in the shear layer, but perhaps the roll up of smaller structures in comparison to those in LR and LC. Mi et al. (2007) performed PIV measurements on unbounded jets issuing from round sharp-edged plates. (Their jet Reynolds number based on orifice diameter d was 72000 as compared with 12000 for the case in Fig. 10(c).) The peak values of u_{rms}/U_{jet} measured by Mi et al. were slightly larger than in the present flow, and the rate of spread in the shear layer was slightly lower. In the present wall-bounded flow, we expect that wall interactions would increase the rate of shear layer growth. Specifically, conservation of mass at each pipe section combined with mass entrainment in the jet causes some mean flow in the negative streamwise direction at large values of r (seen in all cases presented in Fig. 10). This countercurrent effect typically serves to accelerate shear layer growth (Strykowski and Wilcoxon, 1993).

Similar to the LC case, the TC case in Fig. 10(d) reveals significant inward radial velocity downstream of the deformed orifice, and the mean streamwise component is lower at the centerline than at the edge of the jet ($r/D \approx 0.16$). The initial profile is broader as a result of orifice area expansion leading to lower local velocity magnitudes. Similar to the TR case, the core of the jet appears relatively undisturbed near the centerline to the limit of the field of view. This difference in behavior (vs. LC and LR) is at least partly explained by the larger initial jet diameter (= the effective

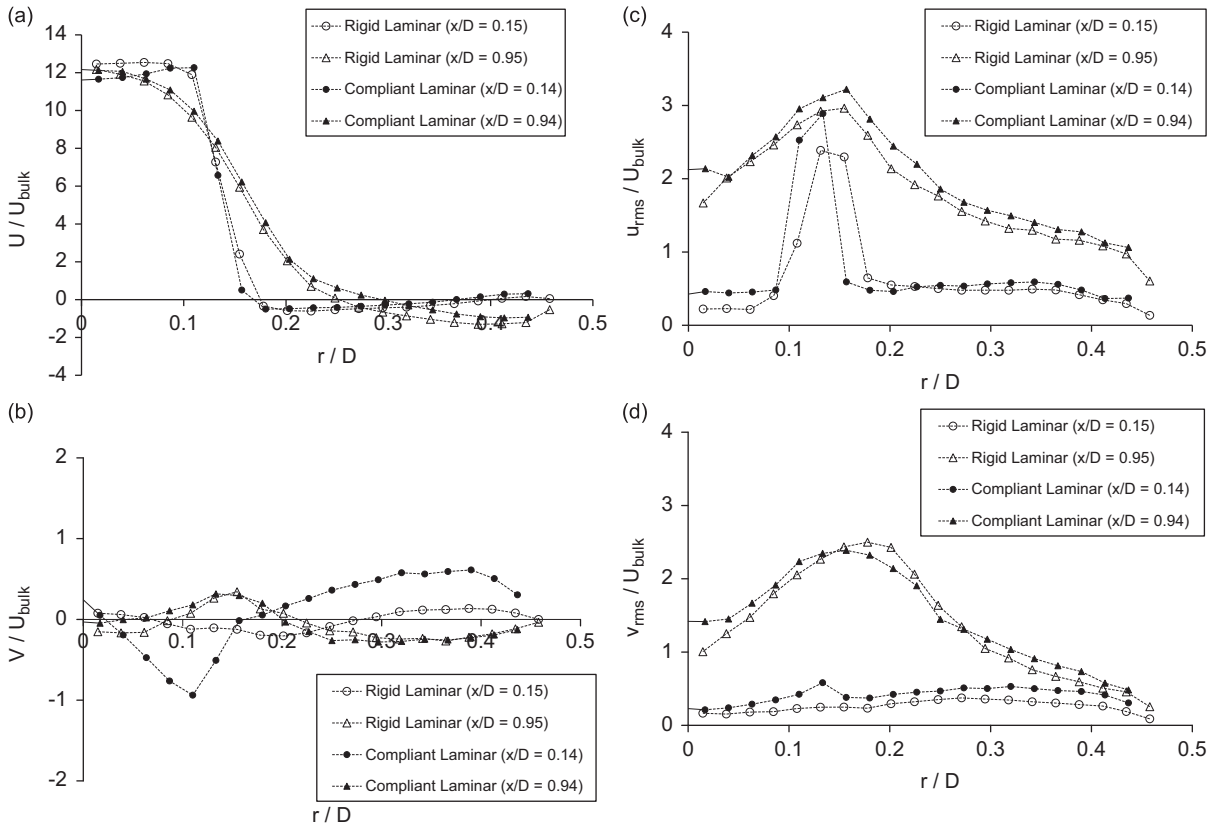

Fig. 11. Mean and rms velocity profiles, Re = 600, $d/D = 0.31$: (a) streamwise mean U, (b) radial mean V, (c) u_{rms}, and (d) v_{rms}.

orifice diameter d_{eff} for this Reynolds number) since shear layer development depends directly on this scale, not D. The u_{rms}/U_{bulk} levels are in general smaller and spread less quickly than in the other three cases presented.

To examine the differences in the downstream flow in more detail, the mean and rms values of the individual velocity components are plotted for all four cases immediately after the orifice exit and further downstream. Figs. 11 and 12 show the profiles resulting from laminar and turbulent upstream conditions, respectively. In both figures, circles and triangles represent the exit and $+0.8D$ (or $+71$ for TC) downstream from the exit locations respectively. Open symbols represent the rigid diaphragm, and closed or solid symbols represent the compliant diaphragm.

In Fig. 11(a), comparing U/U_{bulk} for the laminar rigid and compliant cases, the LR profile (open circles) is initially uniform for $r/D \leq 0.1$, while the curved diaphragm upstream of the LC profile (closed circles) yields higher streamwise velocity near $r/D = 0.1$ than at the centerline. As discussed earlier, at this relatively low Reynolds number, the radial expansion of the orifice is minimal so that the initial width of the jet in these two cases is comparable, although in this view, the shear layer (layer with strong radial velocity gradient dU/dr) appears slightly narrower in the LC case. Further downstream at $x/D = 0.95$, the LC (closed triangles) and LR (open triangles) profiles are very similar. Beyond $r/D = 0.25$, there is evidence of an average reverse flow for both cases indicating a persistence of recirculation to this point. In Fig. 11(b), the plots of V/U_{bulk} emphasize the inward radial flow for $r/D < 0.15$ at $x/D = 0.14$ for the compliant case (closed circles). The inward flow is strongest near $r/D = 0.12$ with a magnitude $\sim U_{bulk}$. Beyond $r/D = 0.15$, the flow initially moves radially outward in the mean for this case (seen also in Fig. 10(b)). In comparison, the mean radial velocity is initially small in the LR case (open circles).

The rms profiles for the LR and LC cases are shown in Fig. 11(c) and (d). Initially, the rms values are small in both cases except in the narrow shear layer near $r/D = 0.13$. Further downstream, both u_{rms} and v_{rms} are large for both cases. The significant radial fluctuations corresponding with the large values of v_{rms} give further evidence of the presence of coherent vortical motions. In general, the u_{rms} values are somewhat higher than the v_{rms} values. Also, u_{rms} values for LC

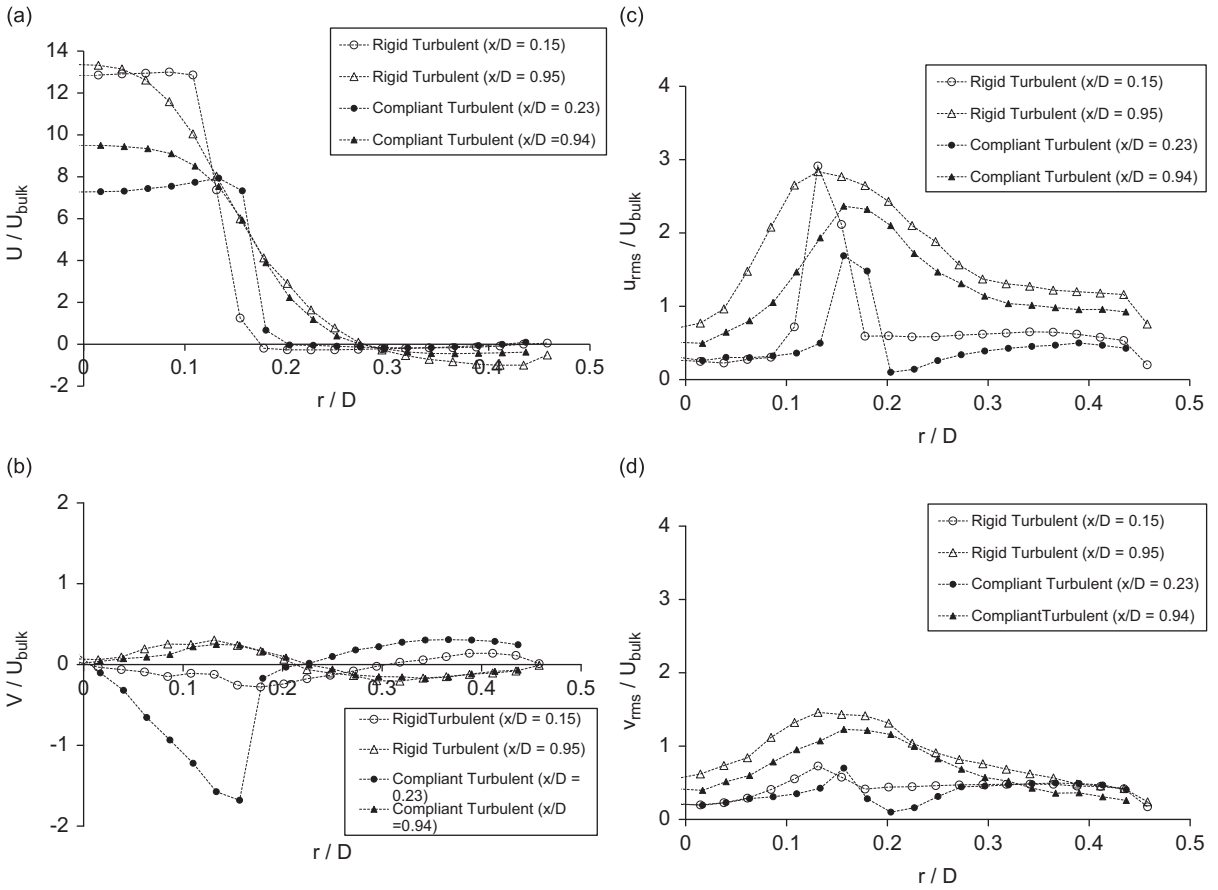

Fig. 12. Mean and rms velocity profiles, Re = 3900, $d/D = 0.31$: (a) streamwise mean U, (b) radial mean V, (c) u_{rms}, and (d) v_{rms}.

are slightly larger than for LR. Notice also that the peaks in the various rms profiles have moved radially outward with increasing streamwise distance.

In Fig. 12(a), U/U_{bulk} is plotted for the higher Reynolds number TR and TC cases. The exit profile for TR (open circles) is indeed narrower than that for TC (closed circles). Also, the mean streamwise profile for TR broadens into a shape similar to that observed for LR at this location (see Fig. 11(a)). It is notable that, because of the significant orifice expansion, the TC profile maintains weaker streamwise velocity magnitudes over its inner portion and correspondingly, weaker reverse velocities over its outer portion. Fig. 12(b) reveals a radial velocity profile for TC (closed circles) that is similar to LC (in Fig. 11(b)): the inward radial velocity increases linearly with increasing radius to the limit of the jet. The peak inward velocity has magnitude $\sim 1.7U_{bulk}$. The outward radial component at larger radii has smaller magnitude than was observed in the LC case (Fig. 11(b)). The TR case yields small values of V at both streamwise locations. The downstream trends observed in Fig. 12(b) are similar to those for LC and LR in Fig. 11(b). For example, at larger r/D values, the mean flow is moving outward at the earlier and inward at the later streamwise location.

At the orifice exit, the streamwise rms component u_{rms}/U_{bulk} (Fig. 12(c)) is small except in a relatively narrow shear layer for both TR (open circles) and TC (closed circles). The peak value for TR is initially larger than that in TC as might be expected because the peak rms value scales with the velocity difference across the shear layer (Pope, 2005) and this velocity difference is larger for TR. Further downstream, each shear layer has broadened, and the TR case yields higher u_{rms} values than the TC case, but both cases have similar magnitudes of v_{rms} (Fig. 12(d)). Unlike the LC and LR cases discussed previously, the rms values at the centerline remain relatively small at the downstream end of the field of view.

In order to quantify a mean vena contracta effect, Fig. 13 plots the streamwise distribution of the quantity U_m/U_c where U_m is the maximum centerline velocity within the field of view, and U_c is the local centerline velocity. The rigid cases LR and TR show very little spatial acceleration in centerline velocity beyond the exit of the orifice. By contrast, the laminar compliant case (LC) shows significant acceleration up to $x/D = 0.3$, and the turbulent compliant case (TC) shows significant acceleration up to $x/D = 0.5$. For these two cases, the quantity U_m/U_c is minimized at $x/D = 0.38$ and 0.56, respectively. Thus, even taking into account the increased axial displacement of the orifice at higher Re, the TC case exhibits acceleration over a longer distance suggesting a longer vena contracta effect. Based on the values of centerline mean velocity, the potential core of the jet appears to be preserved up to $x/D = 0.95$ for both turbulent cases but not for the laminar cases. The behavior of the TR case is similar to that observed in previous experiments on jets by DeOtte et al. (1991) and Mi et al. (2001).

Fig. 14 shows examples of instantaneous velocity vector fields overlaid with contours of swirl strength, which is defined herein as the imaginary part of the eigenvalue of the two-dimensional velocity gradient tensor (Adrian et al., 2000). The swirl strength is normalized by U_{bulk} and pipe diameter D and plotted above a threshold of 50. Regions of positive swirl strength correspond with locations in which flow swirls about an axis normal to the measurement plane. Therefore, they are good indicators of vortex core regions. The instantaneous fields shown were chosen as fairly representative of the many fields acquired for each case, and they highlight some flow features that would affect the mean and rms velocity statistics presented previously.

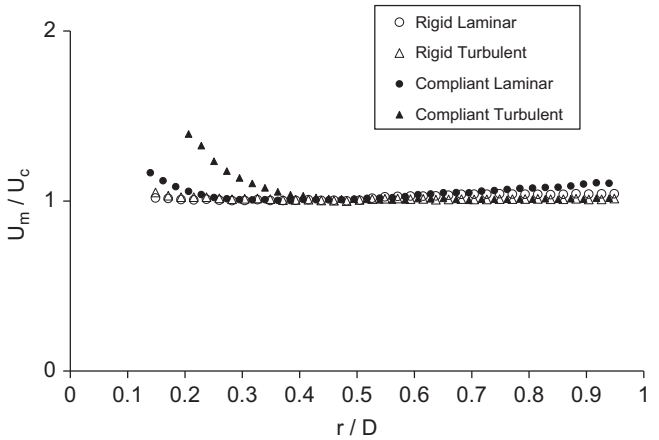

Fig. 13. Inverse mean velocity distribution along the centerline (U_c). U_m is the maximum centerline velocity within the field. Profiles for $d/D = 0.31$.

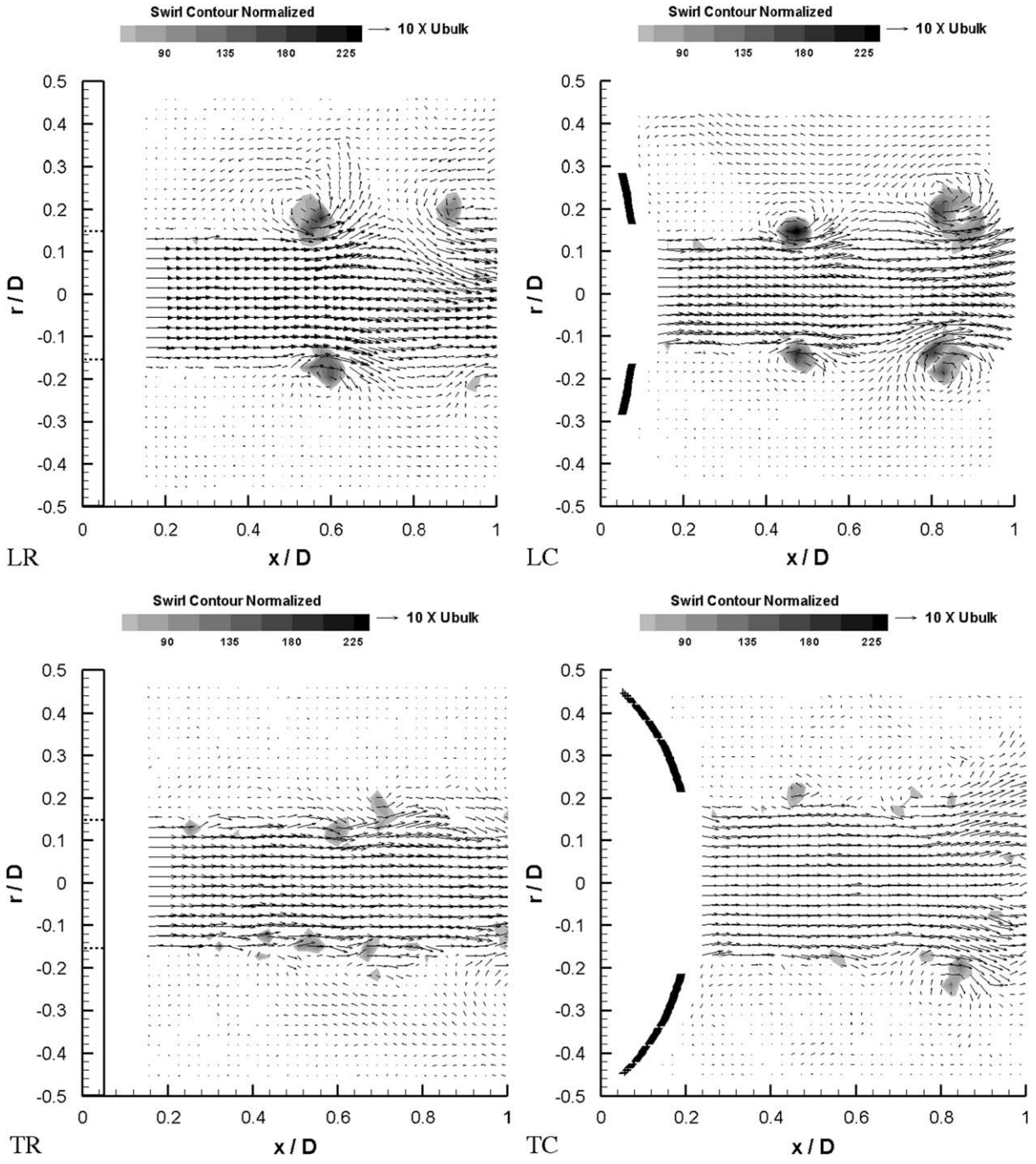

Fig. 14. Instantaneous velocity vector fields with swirl contours for LR ($d/D = 0.31$), LC ($d/D = 0.31$ and $d_{eff}/D = 0.31$), TR ($d/D = 0.31$), and TC ($d/D = 0.31$ and $d_{eff}/D = 0.42$) cases. Swirl is normalized by U_{bulk} and D. Minimum swirl value plotted = 50. Contour increments are 22.5. Based on the pixel displacement accuracy, the uncertainty in a given normalized velocity vector for LR, LC, TR, and TC was 0.22, 0.20, 0.24, and 0.16 times U_{bulk}, respectively.

For Re = 600, the spread in increased rms values occurring near $x/D = 0.5$ for LR and LC (Fig. 10) is consistent with the roll up of relatively large coherent vortex rings, which can be observed in the instantaneous fields in Fig. 14. Both fields show a vortex ring spacing of approximately $0.4D = 1.3d_{eff}$. The rings appear to generate streamwise velocity variations that are felt both at the centerline and at large radii outside of the jet. Although the rings appear reasonably

axisymmetric, three-dimensional variations are also present. Reverse flow is present between the jet and the pipe wall in both flow cases.

The instantaneous fields downstream of the turbulent pipe flow yield qualitatively different results. In the TR case, numerous smaller cores are identified downstream of the orifice by the swirl criterion. Some of the cores appear to be parts of rings because they have a counterpart of similar size and strength on the opposing side of the jet at a similar streamwise location. The streamwise spacing of these cores varies over a range of 0.1–0.35D. The individual cores cause weaker, more localized disturbances compared with the stronger cores in the LC and LR case. In the plot shown, the flow near the jet centerline appears undisturbed by the shear layer to the limit of the field of view ($x/D = 1$). The TC case (Fig. 14(d)) exhibits a wider jet downstream of the expanded orifice. As in the TR case, a number of small, relatively weak cores are present, but it is unclear whether they are parts of coherent rings or helical structures. In most of the TC instantaneous fields, the flow at the centerline appears largely undisturbed all the way to $x/D = 1$.

Downstream mean velocity vectors for a larger orifice size ($d/D = 0.69$) are plotted along with u_{rms}/U_{bulk} contours in Fig. 15(a). In this case, the pipe Reynolds number is larger (8800) in order to generate significant deformation of the diaphragm. The statistical uncertainties in the averaged quantities U and u_{rms} measured near the jet centerline were $0.0025U_{bulk}$ and $0.002U_{bulk}$, respectively. Fig. 15(b) shows the velocity profiles at $x/D = 0.15$ and 0.98. The jet profile is flatter at the exit ($x/D = 0.15$) than in the LC and TC cases with $d/D = 0.31$ and has a peak value of $U/U_{bulk} = 2$. As with the $d/D = 0.31$ cases, there is measurable inward radial velocity near the diaphragm lip and a shear layer develops with increasing streamwise distance. Since u_{rms} scales with the local mean velocity which is $\sim 2U_{bulk}$, the u_{rms} contours are plotted to lower limits than those in Fig. 10. For comparison purposes, the lower limit in Fig. 15(a) is set at 2/7 that shown in Fig. 10(d) ($d/D = 0.31$) where the local mean velocity was $\sim 7U_{bulk}$. When the two cases are compared, then, we can see that the two shear layers spread at similar rates, but the shear layer for $d/D = 0.69$ interacts more quickly with the pipe wall as would be expected. Individual profiles of the mean streamwise and radial components (Fig. 15(b)) indicate a persistence of reversing flow at $x/D = 0.98$, but no mean radial velocity.

The rms plots in Fig. 15(c) show low values immediately downstream of the orifice (open symbols). The profile of u_{rms}/U_{bulk} contains a sharp peak centered at $r/D = 0.35$ that corresponds with the location of strong mean velocity gradient dU/dr in Fig. 15(b). At $x/D = 0.98$, both u_{rms} and v_{rms} are significant at larger radii, indicative of the shear layer there. Both quantities remain low for $r/D < 0.2$, however, suggesting a relatively steady core region. Again, this can be contrasted with the TC case at $x/D = 0.95$ (see Fig. 12(c) and (d)) in which rms values are elevated at the centerline, and the shear layer is focused closer to the centerline. The instantaneous vector field in Fig. 15(d) shows coherent vortex cores near $x/D = 0.45$ and $x/D = 0.8$.

3.5. Velocity spectra

Fig. 16 shows spectral measurements resulting from the hot-film anemometry time records for the LR, LC, TR, and TC cases. In the plots, the power spectral density function is normalized using frequency f and signal variance σ^2. Both cases with upstream laminar flow (LC and LR) yield a distinct and dominant peak at 9.8 Hz, indicating indeed that vortices are developing with a regular frequency and spacing. In both laminar cases, there is very little energy above 40 Hz. The two cases with turbulent upstream conditions (TR and TC) yield broader, relatively featureless spectra that extend to higher frequencies. The TC case, in which the orifice area was larger and jet mean velocity values were lower, contains more energy at lower frequencies than the TR case as expected.

If the peak frequency of 9.8 Hz observed for LR and LC is normalized using the effective orifice diameter and the mean velocity through the orifice, the corresponding Strouhal number ($St = fd_{eff}/U_{mean}$) is 0.34 for both cases. This value of St corresponds closely with the frequency of the jet column mode observed, although typically further downstream, in free jets exiting contoured nozzles (Crow and Champagne, 1971; Danaila et al., 1997). The value $St = 0.34$ can be interpreted as the dimensionless passage frequency of vortex rings at a given streamwise location. If, for example, the vortex passage frequency is 9.8 Hz, and the vortex passage velocity is $\sim 0.5U_{mean}$, then the streamwise vortex spacing would be the velocity divided by the frequency or $0.5D$ ($= 1.6d_{eff}$) which is comparable to the spacing observed in the instantaneous PIV fields (Fig. 14(a) and (b)).

When the power spectral density is replotted versus. Strouhal number as defined above (see Fig. 17), the range of energy-containing frequencies observed for TR falls within the envelopes spanned by the two lower speed cases (LC and LR) suggesting some similarity in streamwise vortex spacing (although the TR case favors a range of frequencies rather than a single frequency). The TC case, however, yields Strouhal numbers with higher values, suggesting the presence of eddies or fluctuations with smaller streamwise spacing and that the jet column mode has not yet developed. A spatial delay in jet development could be expected in the TC case for several reasons: due to the axial deformation of the diaphragm, this jet initiates further downstream than in the other cases studied; the effective jet diameter is larger; and the jet exhibits the longest vena contracta.

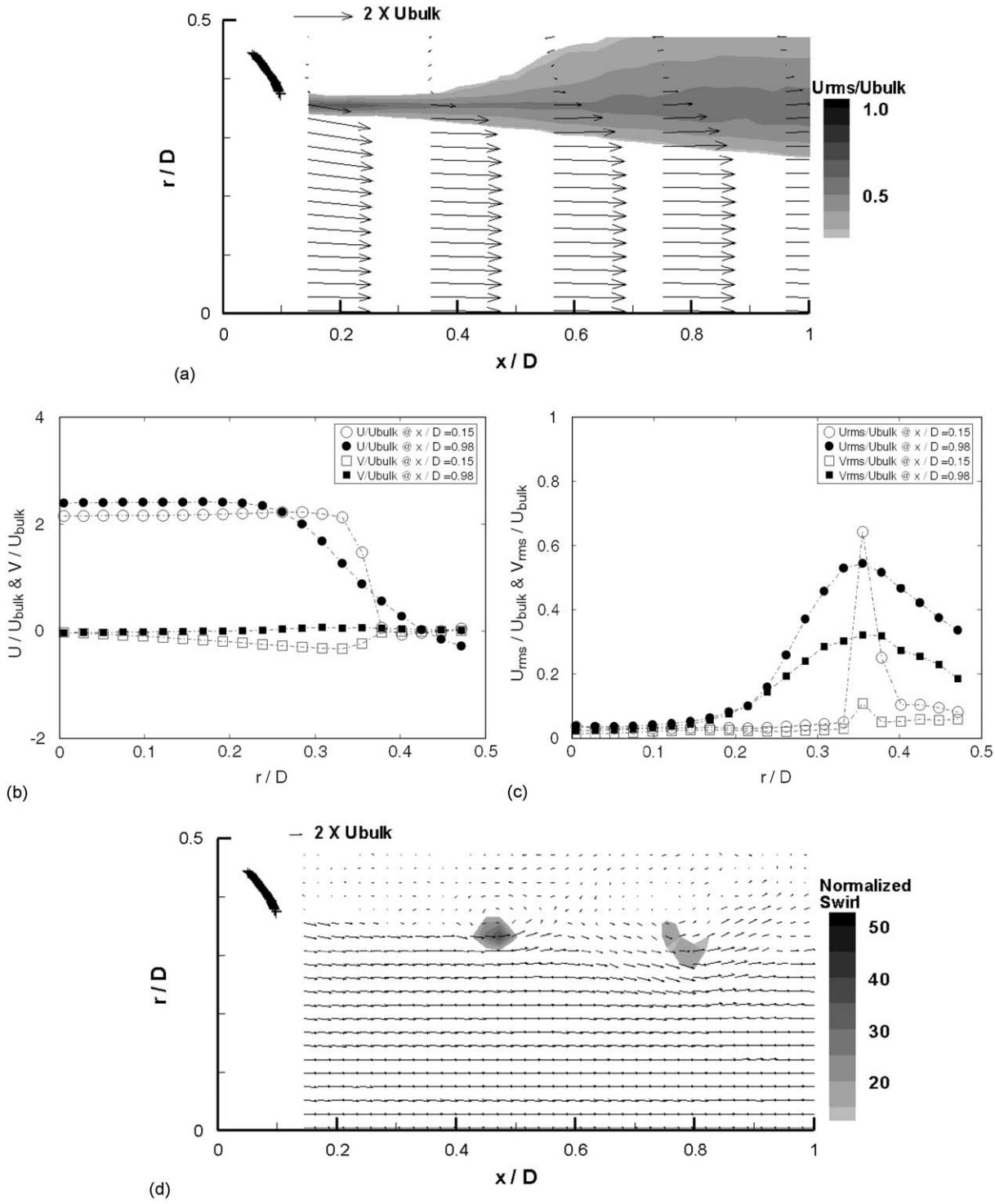

Fig. 15. Re = 8800, $d/D = 0.69$. (a) Mean velocity vector field with u_{rms}/U_{bulk} contours, lowest contour plotted = 0.28. Contour increments are 0.11 (b) mean velocity profiles, (c) rms velocity profiles, and (d) instantaneous velocity vector field with normalized swirl contours. Vector uncertainty is 0.03. Lowest swirl value plotted = 14. Contour increments are 5.

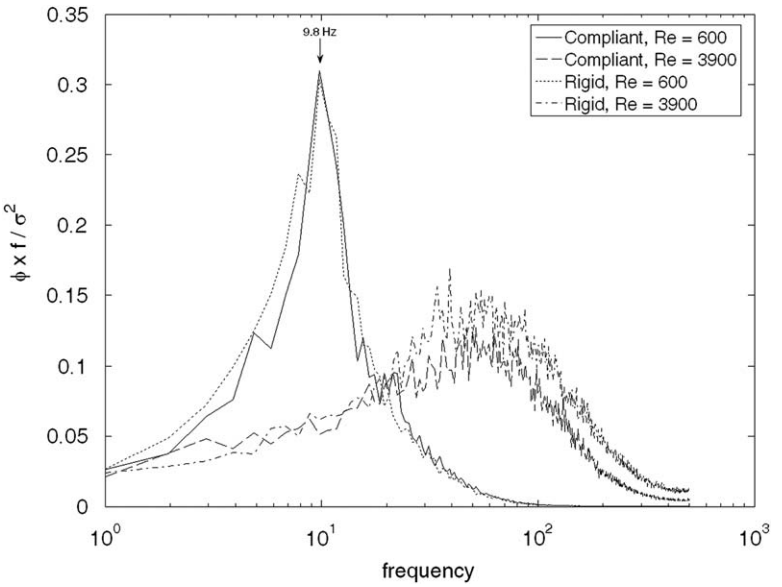

Fig. 16. Power spectra of the flow measured at $x/D = 0.9$ and radial location of strongest fluctuation energy. All cases are for $d/D = 0.31$. The variance in the data is σ^2.

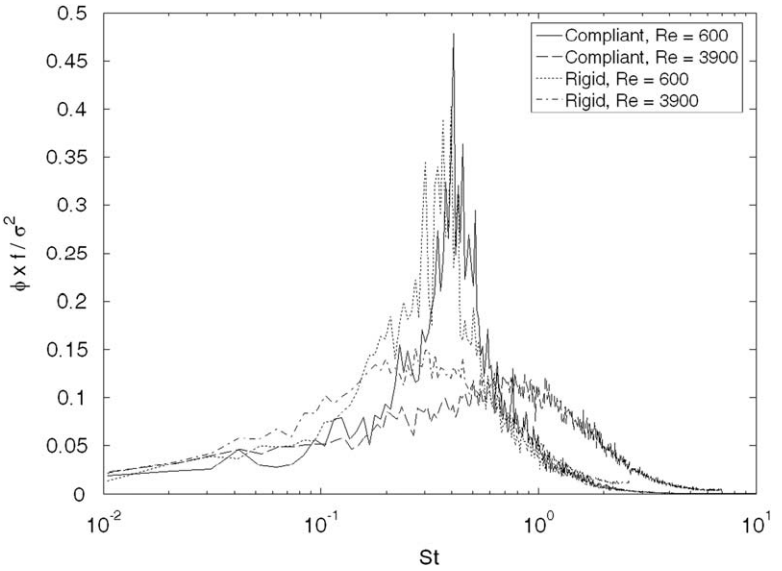

Fig. 17. Power spectra vs. Strouhal number based on deformed orifice diameter and mean velocity through orifice. $St = (f^* d_{eff})/U_{mean}$. Signals measured at $x/D = 0.9$ and radial location of strongest fluctuation energy. All cases are for $d/D = 0.31$. The variance in the data is σ^2.

4. Summary and conclusions

In this paper, we have presented detailed results of material properties, deformation, and fluid velocity for flow through a deformable diaphragm. The upstream flow was controlled by adjusting Reynolds number (volumetric flow rate) while the material modulus was varied to control the degree of diaphragm deformation at a given Reynolds number. Both the material compliance and Reynolds number affect the diaphragm deformation state. At low Reynolds number (Re = 600), the diaphragm deflects downstream into a concave shape, but orifice area expansion is minimal. At higher Reynolds number (Re = 3900), the material compliance results in significant axial deflection as well as expansion

of the orifice area which leads to lower pressure drops compared with flow through a rigid orifice. The pressure drop across the diaphragm appears to dominate shear forces along its surface resulting in a concave (as opposed to convex) deformation for all compliant cases studied including orifice diameters up to $0.69D$.

The effect of diaphragm deformation on downstream flow was also documented. Significant inward radial velocity is present immediately downstream of the deformed diaphragms and absent for the rigid cases. This inward flow was associated with vena contracta in the compliant cases. For low Reynolds number, laminar upstream flow conditions, the rigid and slightly deformed compliant diaphragms both supported the formation of relatively large scale vortices with passage frequency of $St = 0.34$. Ensemble-averaged velocity statistics showed that local rms profiles were similar in both cases although the profiles spread faster in the radial direction, and the magnitudes were slightly larger in the compliant case. For higher Reynolds number, turbulent upstream conditions, the compliant diaphragm deformed significantly, and the orifice area increased by 75% compared with the rigid diaphragm area. The orifice area expansion led to a jet that was initially wider and slower than the comparable rigid case. Since rms values typically scale on the mean jet velocity, the magnitudes were lower in the compliant case. Vortical structures forming immediately downstream of each orifice were typically less organized and more closely spaced than in the cases with laminar upstream conditions. While the range of Strouhal numbers observed in the shear layer of the turbulent rigid case collapsed well with the laminar cases, the range observed in the turbulent compliant case was higher indicating delayed development of the jet downstream.

The experimental data presented can be used to validate fluid–structure interaction codes in which substantial structural deformation and strain are present along with complex flow at significant Reynolds numbers. The experimental geometry and parameters were chosen to be as simple as possible while including these effects. The experimental results are currently being compared against a three-dimensional extension of the code developed by Lui et al. (2007) that overlays deforming and fixed grids needed for the deforming valve and the pipe flow, respectively. As described in the Introduction, an eventual application for such a code includes the modeling of flows through heart valves, which exhibit structural strain and deflection as well as jetting fluid surrounded by recirculation zones. Clearly the code for the heart valve application would need to include additional complexity related to more complicated geometry, material properties of the leaflets and valve root, and pulsating flow conditions, and these effects are not addressed herein. At the same time, it is our hope that the present results will be useful in development of models for additional applications including flows through elastic tubes and expandable bladders as well as industrial flows through deformable orifices used, for example, to regulate flow rate or liquid breakup in sprays.

Acknowledgment

The authors gratefully acknowledge support for this work from NIH (NIH/NHLBI 1R01HL071538-01).

References

Adrian, R.J., Christensen, K.T., Liu, Z.C., 2000. Analysis and interpretation of instantaneous turbulent velocity fields. Experiments in Fluids 29, 275–290.

Carmody, C.J., Burriesci, G., Howard, I.C., Patterson, E.A., 2006. An approach to the simulation of fluid–structure interaction in the aortic valve. Journal of Biomechanics 39, 158–169.

Cheng, R., Lai, Y.G., Chandran, K.B., 2003. Two-dimensional fluid–structure interaction simulation of bileaflet mechanical heart valve flow dynamics. Journal of Heart Valve Diseases 12 (6), 774–780.

Clark, R.E., 1973. Stress–strain characteristics of fresh and frozen human aortic and mitral leaflets and chordae tendinae: implications for clinical use. Journal of Thorac and Cardiovascular Surgery 66, 202–208.

Crow, S.C., Champagne, F.H., 1971. Orderly structure in jet turbulence. Journal of Fluid Mechanics 48, 547–591.

Danaila, I., Dusek, J., Anselmet, F., 1997. Coherent structures in a round, spatially evolving, unforced, homogeneous jet at low Reynolds number. Physics of Fluids 9, 3323–3341.

Dasi, L.P., Ge, H., Simon, A., Sotiropolous, F., Yoganathan, A.P., 2007. Vorticity dynamics of a bileaflet mechanical valve in an axisymmetric aorta. Physics of Fluids 19, 067105.

de Hart, J., Peters, G.W.M., Schreurs, P.J.G., Baaijens, F.P.T., 2000. A two-dimensional fluid–structure interaction model of the aortic heart valve. Journal of Biomechanics 33, 1079–1088.

de Hart, J., Peters, G.W.M., Schreurs, P.J.G., Baaijens, F.P.T., 2003. A three-dimensional computational analysis of fluid–structure interaction in the aortic valve. Journal of Biomechanics 36, 103–112.

DeOtte, R.E., Morrison, G.L., Panak, D.L., Nail, G.H., 1991. 3-D laser Doppler anemometry measurements of the axisymmetric flow field near an orifice plate. Flow Measurement and Instrumentation 2, 115–123.

Dumont, K., Stijnen, J.M., Vierendeels, J., Vosse, F.N.v.d., Verdonck, P., 2004. Validation of fluid–structure interaction model of a heart valve using dynamic mesh method in fluent. Computer Methods in Biomechanics and Biomedical Engineering 7, 139–146.

Kaminsky, R., Dumont, K., Weber, H., Schroll, M., Verdonck, P., 2007. PIV validation of blood–heart valve leaflet interaction modeling. International Journal of Artificial Organs 30, 640–648.

Keane, R.D., Adrian, R.J., 1990. Optimization of particle image velocimeters. Part I: double pulsed systems. Measurement Science and Technology 1, 1202–1215.

Lemmon, J.D., Yoganathan, A.P., 2000. Three-dimensional computational model of left heart diastolic function with fluid–structure interaction. ASME Journal of Biomechanical Engineering 122, 109–117.

Lui, K., Radhakrishnan, H., Barocas, V.H., 2007. Simulation of flow around a thin flexible obstruction by means of a deforming grid overlapping a fixed grid. International Journal of Numerical Methods in Fluids, doi:10.1002/fld.1552.

Mavrilas, D., Missirlis, Y., 1991. An approach to the optimization of preparation of bioprosthetic heart valves. Journal of Biomechanics 24 (5), 331–339.

Mi, J., Kalt, P., Nathan, G.J., Wong, C.Y., 2007. PIV measurements of a turbulent jet issuing from round sharp-edged plate. Experiments in Fluids 42, 625–637.

Morrison, G.L., 2003. Euler number based orifice discharge coefficient relationship. Journal of Fluids Engineering 125, 189–191.

Perry, R.H., Green, D.W., Maloney, J.O., 1984. Perry's Chemical Engineer's Handbook, sixth ed., pp. 5–15.

Pope, S.B., 2005. Turbulent Flows. Cambridge University Press, Cambridge.

Stein, P., Sabbah, H.N., 1976. Turbulent blood flow in the ascending aorta of humans with normal and diseased aortic valves. Circulation Research 39, 58–65.

Stijnen, J.M.A., Hart, j.d., Bovendeerd, P.H.M., Vosse, F.N.v., 2004. Evaluation of a fictitious domain method for predicting dynamic response of mechanical heart valve. Journal of Fluids and Structures 19, 835–850.

Strykowski, P.J., Wilcoxon, R.K., 1993. Mixing enhancement due to global oscillation in jets with annular counterflow. AIAA Journal 3, 564–570.

Thubrikar, M., 1990. The Aortic Valve. CRC, Boca Raton.

Wereley, S., Gui, L., 2001. PIV measurement in a four-roll-mill flow with a central difference image correction (CDIC) method. In: 4th International Symposium on Particle Image Velocimetry, September 17, Göttingen, Germany.

Yoganathan, A.P., Chandran, K.B., Sotiropoulos, F., 2005. Flow in prosthetic heart valves: state-of-the-art and future directions. Annals of Biomedical Engineering 33 (12), 1689–1694.